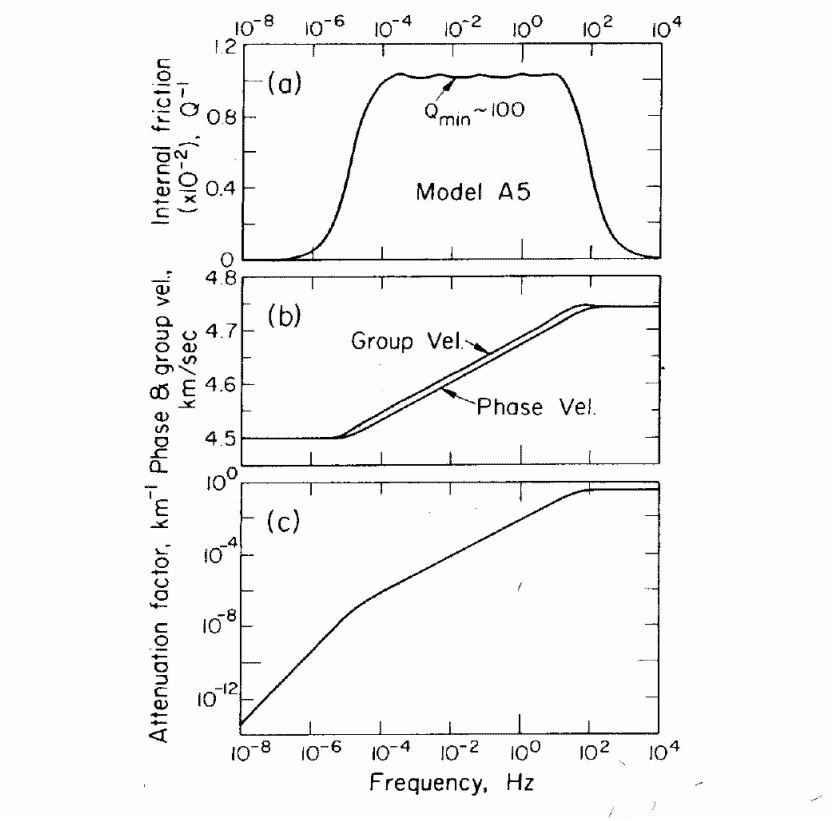

Figure 1: (a) Internal friction (Q^{-1}), (b) phase and group velocity dispersion, and (c) attenuation coefficient as functions of frequency. From **?**.

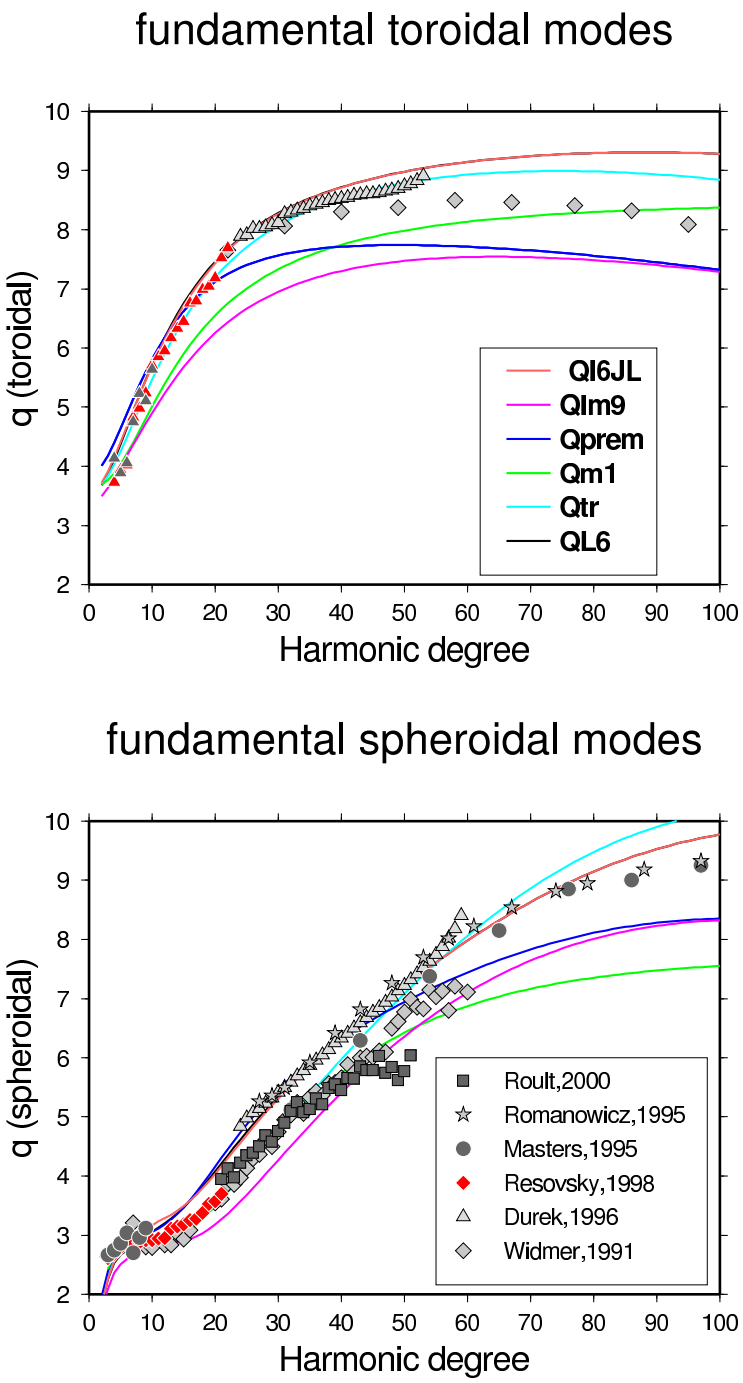

Figure 2: Fundamental mode Q measurements obtained using either a standing mode approach (**???**) or a propagating surface wave approach (**??**). Note the discrepancy between the two approaches in the frequency band where both methods can be applied. Also shown are fits to the data for several models of Q_μ shown in Figure 3. Top: toroidal modes; Bottom: spheroidal modes. Data are from the REM website (http://mahi.ucsd.edu/Gabi/rem.dir/rem.home.html).

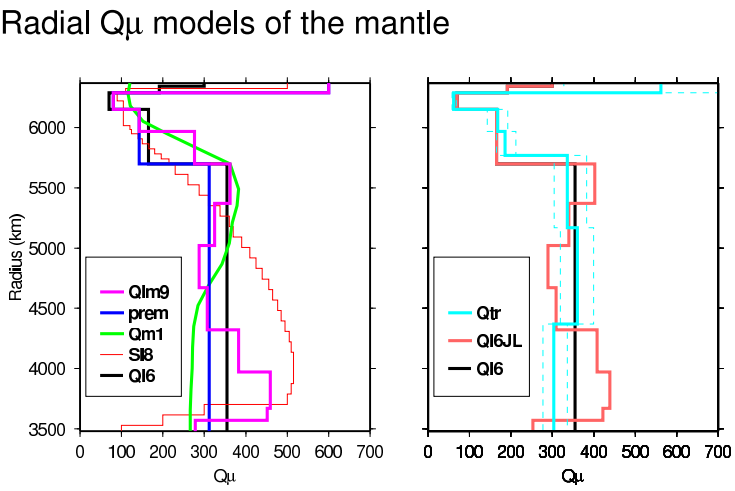

Figure 3: Radial models of Q_μ in the mantle. Left panel: models QM1 (**?**); SL8 (**?**); PREM (**?**); Ql6 (**?**); and Qlm9 (**?**). PREM and QL6 fit fundamental mode Rayleigh wave data, but only QL6 also fits fundamental mode toroidal mode data. Models Qlm9 and QM1 have higher Q in the transition zone. Right panel: Qtr: most probable model and 2-sigma standard deviations (broken line) from the work by **?**, compared to Ql6 and a preliminary model which fits both ScS/S amplitude data and fundamental mode surface wave data (Lawrence, personal communication).

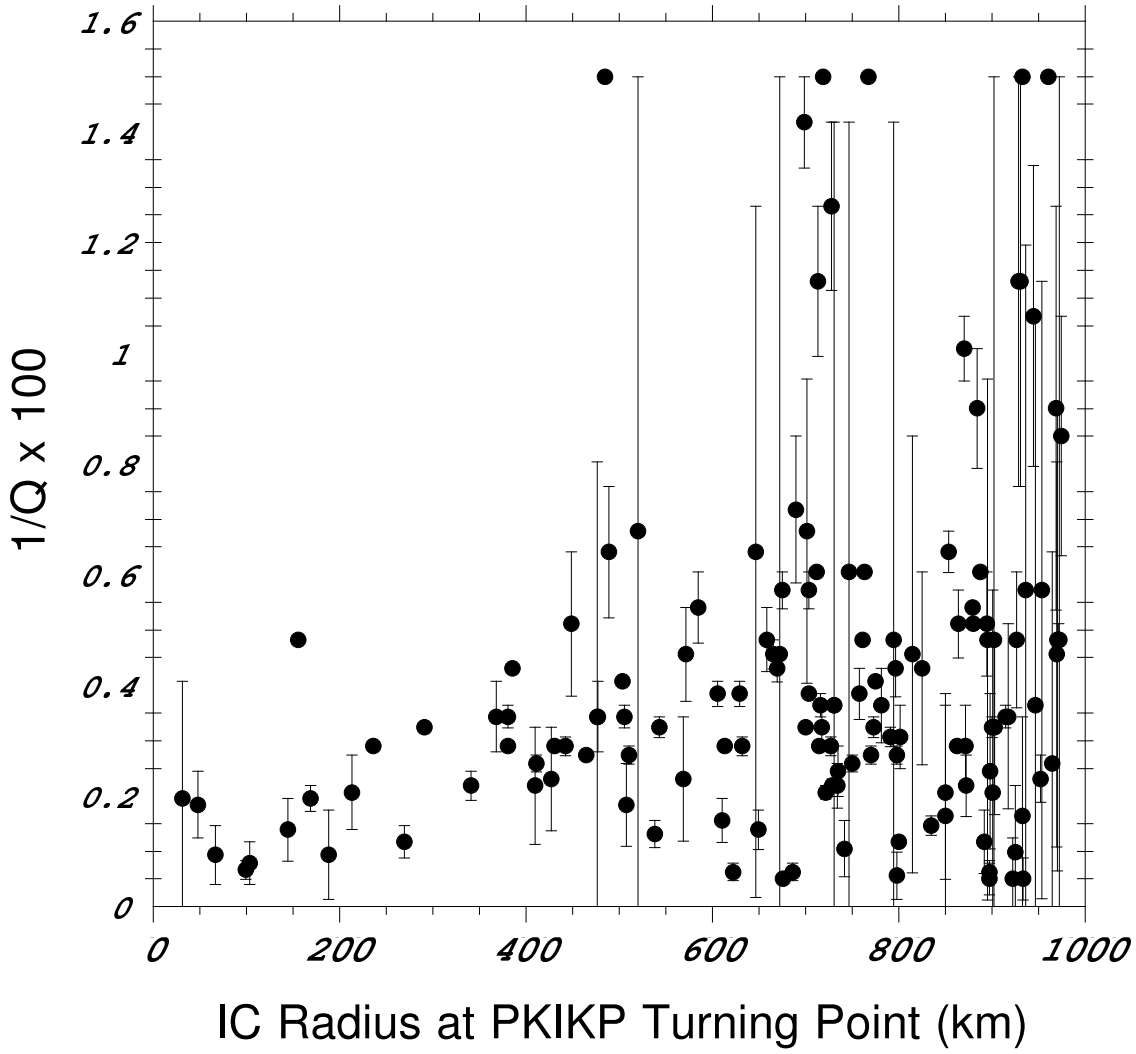

Figure 4: Observed attenuation of $PKP(DF)$ waves as a function of the turning radius of the ray. Reproduced from **?**.

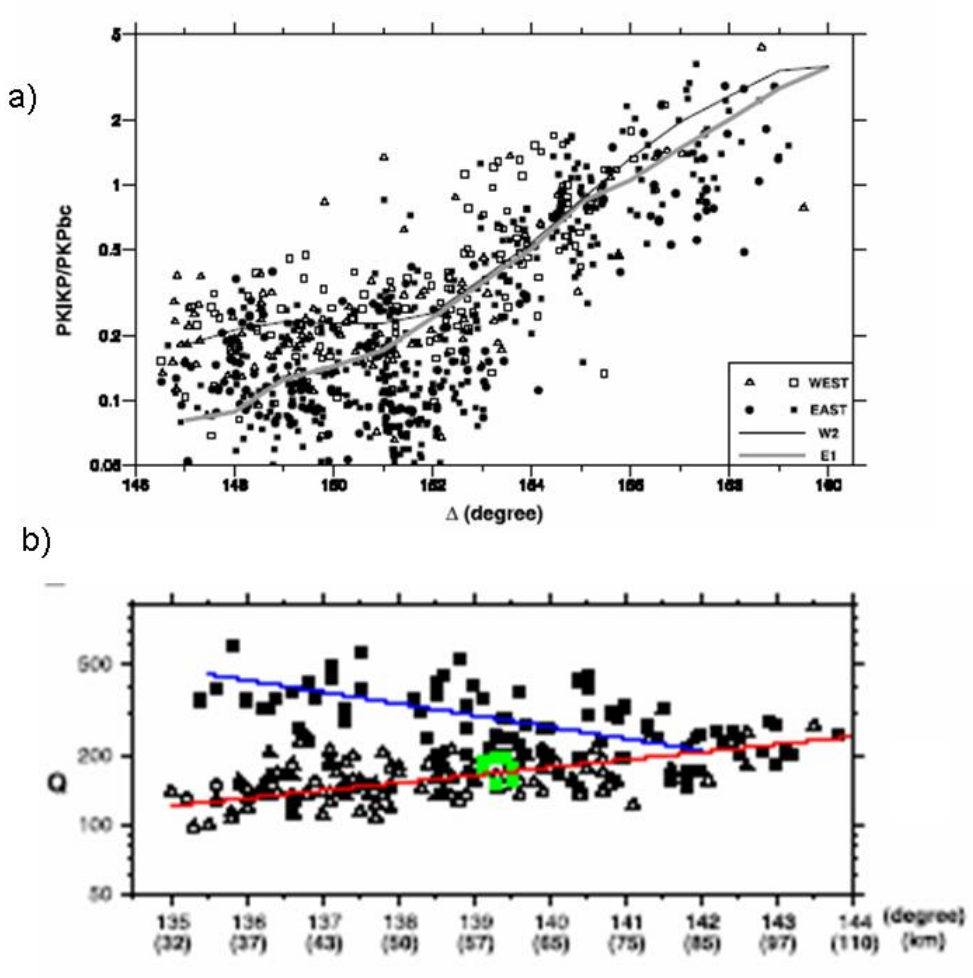

Figure 5: Hemispherical variations of Q in the inner core. Top: Variations of amplitude ratios of $PKIKP/PKP(BC)$ as a function of distance and predictions of Q models for the Western (W2) and Eastern (E1) hemispheres (from Yu and Wen, 2006). Bottom: Q measurements as a function of distance from amplitude ratios of $PKIKP/PKiKP$ showing differences between the western (triangles) and eastern (squares) hemispheres (from **?**.

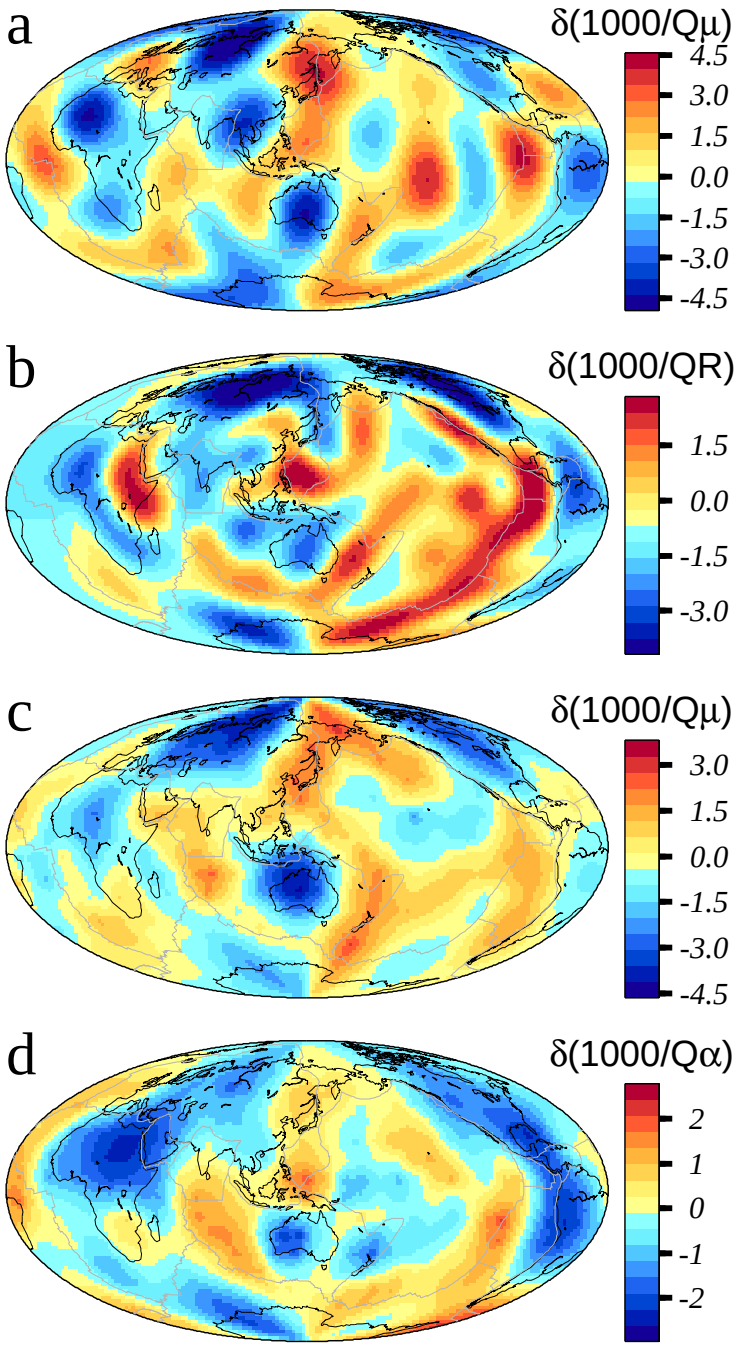

Figure 6: Comparison of global Q models in the uppermost mantle. (a) $QRLW8$ model (**?**) from inversion of three component surface wave and overtone waveform data, presented is Q_μ at a depth of 160 km. (b) map at 150 sec of the Rayleigh wave Q model of **?**. (c) Average Q_μ in the depth range 0-250 km from **?**, also from Rayleigh waves. (d) Average variations in Q_α in the first 250 km of the mantle from amplitude ratios of P and PP (**?**). Some of the differences observed may be due to the different depth ranges sampled: in models (a), (c) and (d), the global ridge and back-arc systems all stand out as low Q_μ features, whereas the atlantic ridge is not as prominent in model (b), while the red sea region lights up more strongly. This may be due to the fact that (b) has not been inverted with depth, and therefore may include some effects of structure deeper than 250 km.

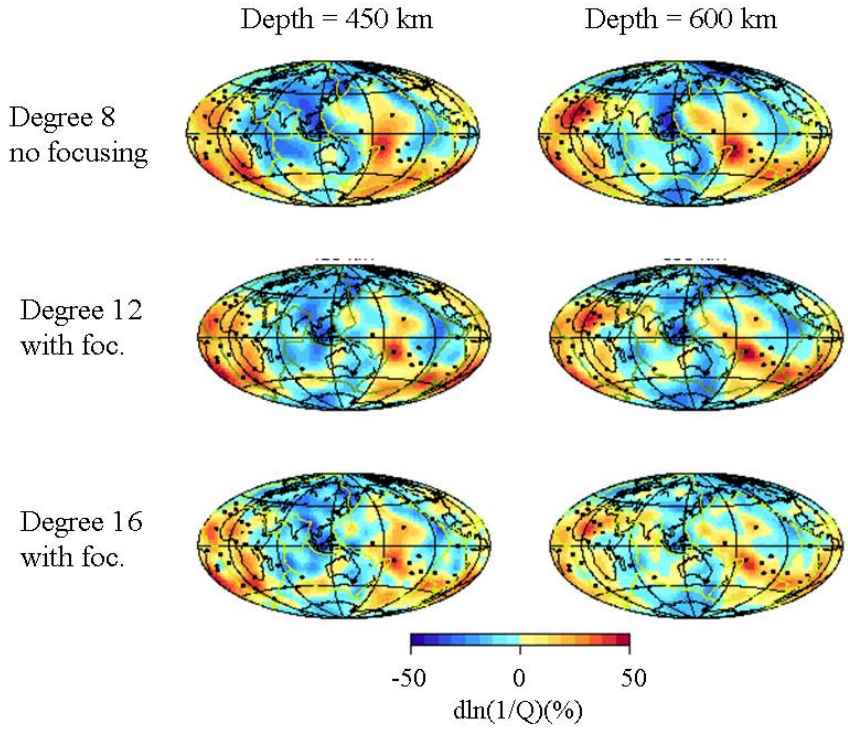

Figure 7: Lateral variations of Q_β in the upper mantle transition zone. Top: Degree 8 Model QRLW8 (**?**). In this relatively low degree model, no corrections for elastic focusing have been included. Middle/Bottom: inversion of the same three component long period seismograms for a degree 12 model (middle) and a degree 16 model (bottom). In both cases, the waveforms have been corrected for focusing effects before inversion, using an asymptotic higher order formalism (**?**). The main features of these models, namely strong low Q anomalies in the south Pacific and under Africa, correlated with the hot spot distribution of (**?**) (black dots) and high Q anomalies under the western Pacific, remain stable, but the low Q features sharpen up in the higher resolution models.

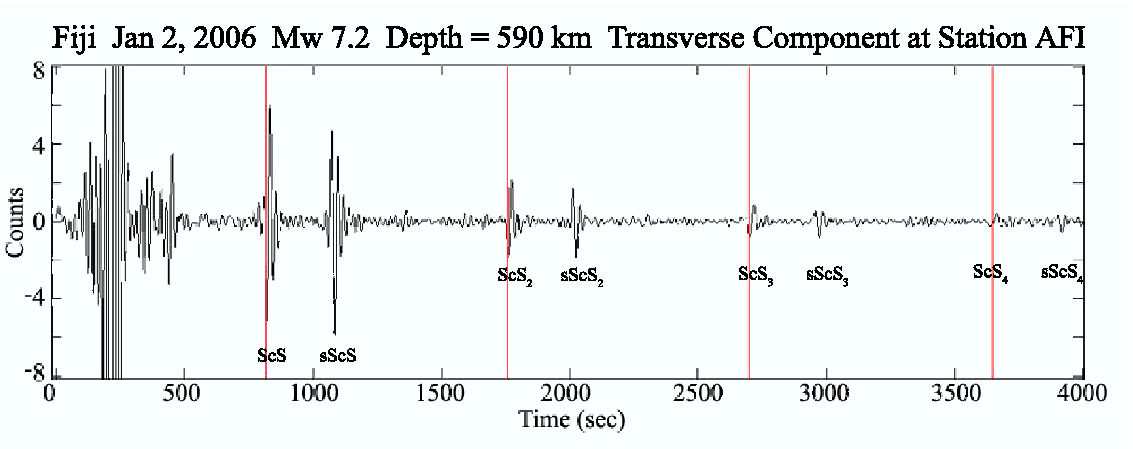

Figure 8: Example of multiple ScS record for a deep earthquake in the Fiji Islands, showing clear multiples out to ScS_4 as well as their depth phases. *Courtesy of Ved Lekic.*

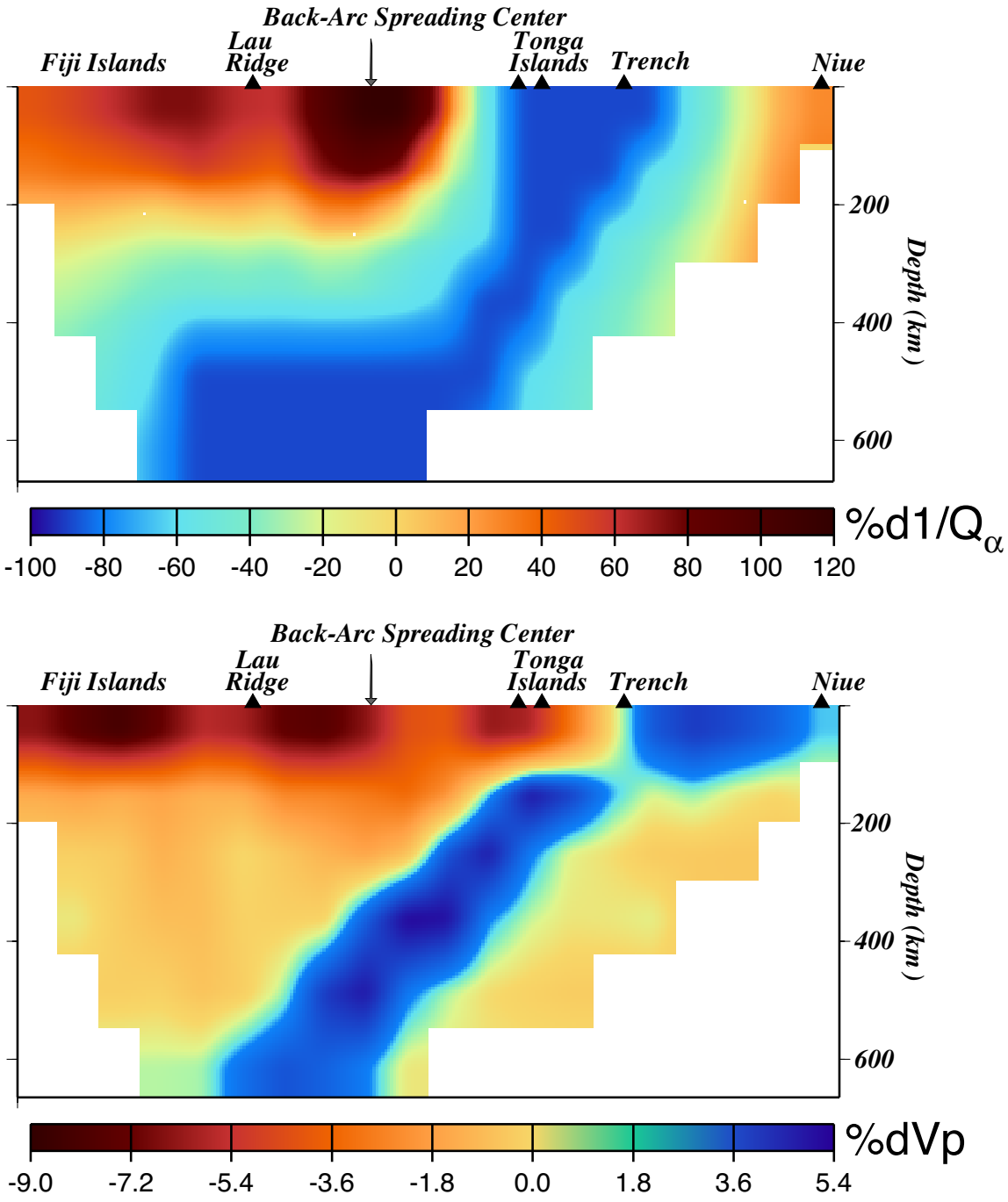

Figure 9: Cross section illustrating ateral variations of structure in the Lau Back Arc Basin (reproduced from **?**). Top: attenuation; bottom: velocity (V_p).